MATERIALS SCIENCE

Tuning peptide self-assembly by an in-tether chiral center

Kuan Hu,[1,2]* Yixiang Jiang,[1]* Wei Xiong,[3] Hu Li,[4] Pei-Yu Zhang,[5] Feng Yin,[1] Qianling Zhang,[6] Hao Geng,[1] Fan Jiang,[1†] Zhou Li,[2†] Xinwei Wang,[3†] Zigang Li[1†]

The self-assembly of peptides into ordered nanostructures is important for understanding both peptide molecular interactions and nanotechnological applications. However, because of the complexity and various self-assembling pathways of peptide molecules, design of self-assembling helical peptides with high controllability and tunability is challenging. We report a new self-assembling mode that uses in-tether chiral center-induced helical peptides as a platform for tunable peptide self-assembly with good controllability. It was found that self-assembling behavior was governed by in-tether substitutional groups, where chirality determined the formation of helical structures and aromaticity provided the driving force for self-assembly. Both factors were essential for peptide self-assembly to occur. Experiments and theoretical calculations indicate long-range crystal-like packing in the self-assembly, which was stabilized by a synergy of interpeptide π-π and π-sulfur interactions and hydrogen bond networks. In addition, the self-assembled peptide nanomaterials were demonstrated to be promising candidate materials for applications in biocompatible electrochemical supercapacitors.

INTRODUCTION

Molecular self-assembly of short peptides into well-ordered nanostructures is a cornerstone of advanced bionanomaterial fabrication (*1*–*3*). It has been used in a variety of applications, including in biomedical (*4*, *5*), optical engineering (*6*), and electronic nanotechnology applications (*7*). Peptide self-assembly is complicated, because peptides display significant variation in their sequences as well as secondary structures (*8*). Assemblies of amphiphilic peptides (*9*), β sheets (*10*), collagens (*11*), and diphenylalanine peptides and their analogs (*12*, *13*) have been studied previously. This list could be extended to include specially designed planar cyclic-D, L-peptides (*14*) and foldectures (*15*), which are self-assembled molecular architectures of β-peptide foldamers. However, these peptide self-assemblies are highly sequence-dependent and susceptible to subtle changes in primary structure. Therefore, the de novo design of tunable and controllable peptide self-assembly remains challenging.

Helices are the basic units of protein secondary structures, and more than 60% of protein-protein interactions involve α helices at their interface (*16*). In this context, efforts have been made toward engineering helical peptide self-assemblies. Recently, self-assemblies of specially designed short linear α-helical peptides were demonstrated to form hollow vesicles (*17*) or two-dimensional nanostructures (*18*). Gazit *et al.* reported a constrained single heptad repeat peptide that could form functional superhelical assemblies (*19*). However, linear peptides are highly flexible, and their secondary structures can be significantly interfered with by subtle perturbations (*20*). Recently, a head-to-tail cyclized helical short peptide was reported to self-assemble through the incorporation of hydrophobic residues (*21*). However, head-to-tail cyclization of helical peptides is sequence-dependent, thus limiting the residue scope for assembly.

By contrast, side-chain–to–side-chain cross-linked helical peptides have more conformational stability than their linear analogs (*22*, *23*). Therefore, we hypothesized that constrained helical peptides are an ideal platform for tunable peptide self-assembly that could minimize environmental perturbations and allow further modifications for fine-tuning the self-assembly for various purposes. We recently demonstrated a precisely positioned in-tether chiral center could induce the backbone peptides into a helical conformation with a preferable absolute configuration generating chirality-induced helical (CIH) peptides, as shown in Fig. 1A (*24*–*26*). We hypothesized that tuning the on-tether substitution group would be a de novo avenue of helical peptide assembly. We envisioned an aromatic substituent that provided π-π intermolecular interactions would serve as a driving force for peptides to self-assemble.

Here, as proof of concept, we demonstrate that CIH peptides assemble into different nanostructures. As shown in Fig. 1A, self-assembling behavior was dominated by the peptide helicity and in-tether functional groups (X). Meanwhile, detailed nanostructures were formed in a sequence-dependent manner, providing significant chemical space for structural and functional tuning. Aromatic phenyl and naphthyl substituents with suitable chirality (***R*** epimers for the helical peptides) facilitated self-assembly. Their nonhelical epimers (***S*** epimers) with aromatic substituents or helical peptides with nonaromatic substituents could not assemble. De novo assembly was demonstrated by the assembly behavior of CIH peptides with different backbone sequences. Notably, the self-assembled bionanomaterials are promising for use in biocompatible electrochemical supercapacitors.

RESULTS

Exploration of stapled peptide self-assembly

Cyclic pentapeptides of Ac-CAAAS$_5$(X)-NH$_2$ (BDCPs; Fig. 1A) were chosen as model peptides to investigate self-assembling behavior. These BDCP peptides did not contain amino acid residues with significant hydrophobic interaction or hydrogen bonding features, but varied in

[1]Key Laboratory of Chemical Genomics, School of Chemical Biology and Biotechnology, Peking University Shenzhen Graduate School, Shenzhen 518055, China. [2]Beijing Institute of Nanoenergy and Nanosystems, Chinese Academy of Sciences, Beijing 100083, China. [3]School of Advanced Materials, Peking University Shenzhen Graduate School, Shenzhen 518055, China. [4]Key Laboratory for Biomechanics and Mechanobiology of the Ministry of Education, School of Biological Science and Medical Engineering, Beihang University, Beijing 100083, China. [5]XtalPi Inc., One Broadway, 9th floor, Cambridge, MA 02142, USA. [6]Shenzhen Key Laboratory of Functional Polymer, College of Chemistry and Environmental Engineering, Shenzhen University, Shenzhen 518060, China.
*These authors contributed equally to this work.
†Corresponding author. Email: lizg@pkusz.edu.cn (Zigang L.); wangxw@pkusz.edu.cn (X.W.); zli@binn.cas.cn (Zhou L.); jiangfan@pku.edu.cn (F.J.)

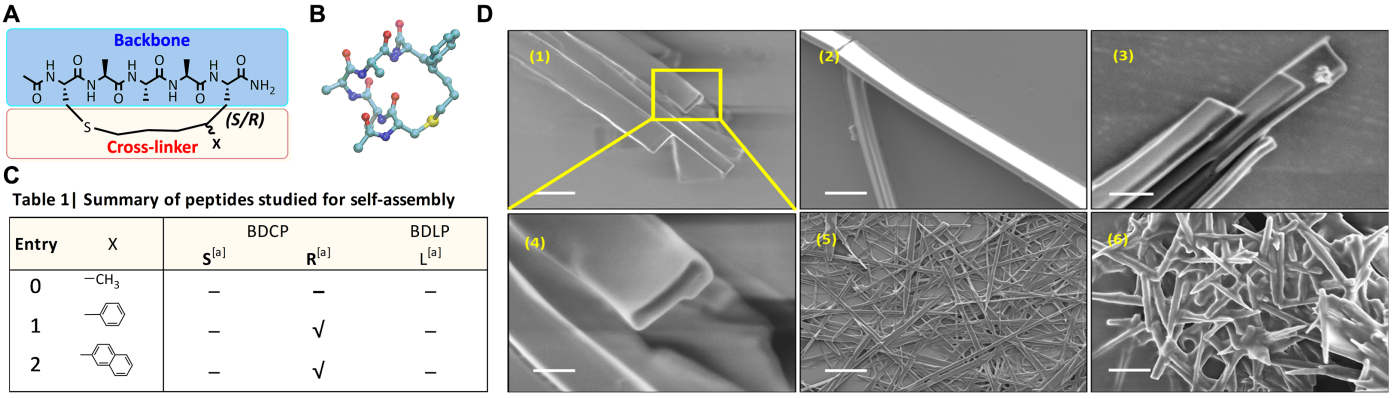

C

Table 1| Summary of peptides studied for self-assembly

Entry	X	BDCP S[a]	BDCP R[a]	BDLP L[a]
0	$-CH_3$	–	–	–
1		–	√	–
2		–	√	–

Fig. 1. Study of BDCP peptides self-assembly. (**A**) Molecular structure of cyclic pentapeptides of Ac-CAAAS$_5$(X)-NH$_2$ (BDCPs). (**B**) Simulated structure of helical BDCP-1-R peptide in water. Figure was adapted from our previous article (*24*). (**C**) Table of peptides tested for self-assembly in H_2O, where "√" and "–" indicate self-assembly was achieved or not achieved, respectively. [a] S and R represents the absolute configuration of the in-tether chiral center in the peptide epimer, and L denotes the peptide is an uncyclized linear peptide (structural details in the Supplementary Materials). (**D**) SEM images of self-assembled BDCP-1-R at various magnifications (images 1 to 5) and BDCP-2-R (image 6). Image 4 is a high-magnification SEM image of the region inside the yellow box in image 1, indicating rectangular cross section. Scale bars, 1 μm (upper left), 3 μm (upper middle), 500 nm (upper right), 200 nm (lower left), 15 μm (lower middle), and 5 μm (lower right).

terms of in-tether chiral center substituents. As shown in our previous work, the helicity of the BDCP peptides was determined by the chiral configuration of the in-tether chiral center, where the R configuration was required for an α-helical structure (*24*). Here, BDCP peptides with three different substituents, where *X* = methyl, phenyl, or naphthyl, were synthesized in two different configurations: R and S. The resulting six purified BDCP peptides consisting of three R/S epimer pairs were characterized using circular dichroism (CD; fig. S1). It was confirmed that only the R-configured BDCP peptides were helical in water, whereas the S-configured epimers were all nonhelical, which is consistent with our previously reported work (*24*, *25*). Figure 1B presents the simulated structure of BDCP-1-R, which was first reported in our previous work (*24*).

Characterization of self-assembly morphology

Self-assembly experiments were performed by placing each type of BDCP peptide (listed in Fig. 1C) -R separately in water at room temperature and then sonicating for 10 min to assist in self-assembly (*27*). Different peptide concentrations were tested to find the optimal condition for self-assembly. Using BDCP-1-R as an example, the concentration ranged from 0.25 to 8 mg/ml. The peptide became fully dissolved when the concentration was below 1 mg/ml, whereas suspended solids were visible when the concentration exceeded 2 mg/ml. These suspended solids were self-assembled BDCP-1 peptides. Under an optical microscope, they appeared needle-shaped and colorless. Further characterization by scanning electron microscopy (SEM) was performed to inspect the morphology of the BDCP-1-R assemblies. Images 1 to 4 in Fig. 1D present the microscopic view of the assemblies, which show that these solid materials were tetragonal-shaped nanobelts or nanotubes tens of micrometers long and hundreds of nanometers to several micrometers wide. Image 5 is a macroscopic view of the assemblies and reveals the assemblies had a large aspect ratio that leads to interweaving of the assemblies.

Conversely, the nonhelical S-configured epimer BDCP-1-S was not able to self-assemble, even when a wider range of peptide concentrations was tested. A similar phenomenon was observed for the naphthyl-substituted BDCP peptide epimers (BDCP-2-R/S), where the helical BDCP-2-R peptide was able to self-assemble into nanostructures (Fig. 1D, image 6), but its nonhelical epimer BDCP-2-S was not. These results indicate that the helical structure was necessary for undergoing self-assembly. The helix constrained the peptide into a compact unit in water, because its peptide chain was much less flexible than those in the random-coil structures of the nonhelical epimers. Additional tests with uncyclized linear peptides (that is, BDLP) with molecular structures that were even more flexible further support these findings. None of the substituted BDLP peptides were able to self-assemble (Fig. 1C).

However, having only an α helix may not be sufficient for self-assembly, and certain functional groups with ample intermolecular interactions are needed to drive assembly. The in-tether substituents of phenyl and naphthyl were critically important for the successful self-assembly of BDCP-1-R and BDCP-2-R, because both aromatic groups were hydrophobic and facilitated adequate intermolecular π-π interactions. These π-π interactions are directional and drive the aromatic rings to stack on one another and, therefore, enable the formation of self-assemblies. If the peptide did not contain an aromatic group, then it could not self-assemble despite its helical content due to a lack of intermolecular π-π interactions to serve as the driving force for self-assembly, as shown by the BDCP-0-R/S pair in Fig. 1C.

After demonstrating the crucial role of both the helical conformations and aromatic substituent groups in self-assembly, the self-assembled nanostructures of the BDCP-1-R peptide were characterized in detail. As shown in Fig. 2A, the left part of the BDCP-1-R peptides clearly had a tubular nanostructure (indicated by the yellow box); however, the right part did not have an obvious tubular shape. This phenomenon may be attributed to the diffusion-limited crystal growth, which was also reported by Lee *et al.* in their short β-peptide foldamer self-assembly system (*15*). On the basis of this mechanism, without any agitation, mass transport on the most rapidly growing face of the crystal is diffusion-limited, resulting in site-dependent growth rate on this crystal face. Diffusion of solute molecules to the outside apexes is easier than that to the central region. During the crystal growth, the concentration of the solution at the center of the crystal growth face decreases until it is no longer supersaturated, leaving only the growth of edges to give tubular structure (*15*). We found that the above explanation can explain the coexistence of nanobelt and nanotubes in our system. The associated electron diffraction (Fig. 2B) reveals a pattern of rings, which suggests that the peptide nanostructures are polycrystalline. Powder x-ray

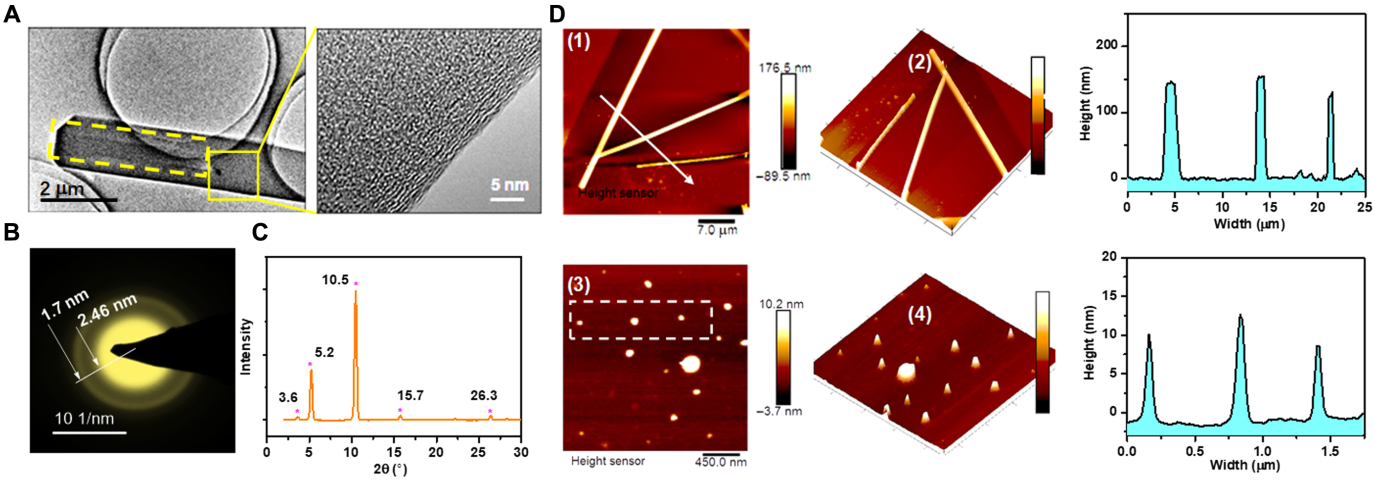

Fig. 2. Characterization of BDCP-1-R peptide nanomaterials. TEM image (**A**), electron diffraction pattern (**B**), and XRD pattern (**C**) of BDCP-1-R peptide nanomaterials. The labels contained a star "*" indicate the diffraction peaks of BDLP-1-R peptide nanomaterials. (**D**) AFM images of the peptide nanomaterials (1) and peptide nanodots (3). Three-dimensional views of (1) and (3) are shown in (2) and (4), respectively. Sectional height plots along the labeled arrows in (1) and (3) are shown on the right.

diffraction (XRD) also revealed sharp diffraction peaks for the nanomaterials (Fig. 2C), indicating long-range ordered crystallites. The diffraction peaks were located at 3.4, 4.44, 5.04, 8.5, 17, and 24.6 Å in lattice spacing, where two were consistent with the transmission electron microscopy (TEM) electron diffraction rings. Atomic force microscopy (AFM) further confirmed the tetragonal shape of the nanostructures, and the average tube height was ~150 nm (Fig. 2D), which is close to the dimension observed by SEM. We also found peptide nanodots in the solution. As shown in Fig. 2D (image 3), these nanodots were about 10 to 20 nm in diameter. A previous report (*28*) suggests that the elementary building blocks for self-assembled peptide nanotubes are nanodots, and the assembling process from dots to tubes is reversible. Perhaps, BDCP-1-R assembled in a similar process involving the formation of nanodots. We also detected the reverse, peptide nanostructure disassembly, upon simply diluting the aqueous solution.

Study of the self-assembly behavior of the assemblies

BDCP-1-R nanomaterials were further characterized by Fourier transform infrared spectroscopy (FTIR) and Raman spectroscopy. FTIR provided information on the chemical nature and secondary structures of the assemblies (*29*). The spectrum for the assemblies (Fig. 3A) contains intense bands for amide I at 1654 cm^{-1} and amide II at 1530 and 1547 cm^{-1}, indicating an α-helical structure (*30*). This observation was further corroborated by the amide III band at 1308 cm^{-1}.

Moreover, the N-H stretching frequencies at 3319 and 3266 cm^{-1} correspond to a hydrogen bond network (Fig. 3A). The Raman spectrum contained a peak at 1652 cm^{-1}, indicating a helical structure for individual peptides and is consistent with the FTIR spectra (Fig. 3B). Therefore, we demonstrated that helical BDCP-1-R is the building block for nanostructure assembly.

To probe the molecular interactions in the nanostructures, ultraviolet (UV)–vis absorption and fluorescence spectroscopy were performed (*31*). UV-vis spectra (Fig. 3C) contained a broad absorption and increased intensity for the BDCP-1-R assemblies compared to the BDCP-1-R monomers, indicating strong π-π interactions between the stacked aromatic groups (*32*). The absorption of the BDCP-1-R monomers was mainly due to the n-π* transitions of the phenyl group, and the phenyl π electrons could interact with a neighboring phenyl group through π-π interactions in the assembled state. Fluorescence spectroscopy was used to measure changes in photoluminescence excitation (PLE) and emission after assembly (*33*). Figure 3D demonstrates that the photoluminescence (PL) and PLE spectra of BDCP-1-R were very different between the peptide nanomaterials (solid lines) and monomers (dash lines).

The red shift in the maximum emission wavelength (red solid line) indicates significant electron delocalization, suggesting strong π-π interactions in the assembly (*31*). Fluorescence imaging was performed on the BDCP-1-R assemblies using standard UV-blue, blue-green, and green-red filters to detect emissions (Fig. 3E). When a suitable excitation wavelength was used, the BDCP-1-R assemblies emitted blue, green, or red fluorescence. The broad range exhibited in the PL spectra by the peptide assemblies indicates they are promising candidates for use in optical and imaging technologies.

Modeling of crystal packing in the self-assembly

The observed sharp XRD peaks indicate long-range ordered packing. We performed crystal structure prediction of the BDCP-1-R peptide by searching peptide conformational and crystal packing degrees of freedom, followed by molecular mechanics and subsequent density functional theory calculations. One low-energy structure fitting the predicted XRD pattern was identified (fig. S2). In this structure (Fig. 4A), each peptide had a backbone and side-chain conformation similar to that in water (Fig. 1B) in agreement with the α-helical structure suggested by our FTIR and Raman spectra (Fig. 3, A and B).

The predicted crystallite structure had alternating polar and nonpolar layers. The nonpolar regions were formed by packing of side-chain tethers in different peptides and driven by aromatic π-π interactions between in-tether phenyl groups and π-sulfur interactions between the phenyl and thioether groups (Fig. 4B). Aromatic side-chain interactions are frequent in protein crystal structures and lead to strong stabilization (*34*). Aromatic-sulfur interactions have also been observed in the crystal structures of many molecules and can help to stabilize peptide helical folding (*35*). The simulation results explain why BDCP-0 peptides lacking aromatic groups cannot self-assemble (Fig. 1C). The π-π interactions of phenyl groups can also explain the observed red shift and broadening of fluorescence and UV-vis spectra upon self-assembly (Fig. 3, C and D). The peptide backbones also packed together to form polar layers by

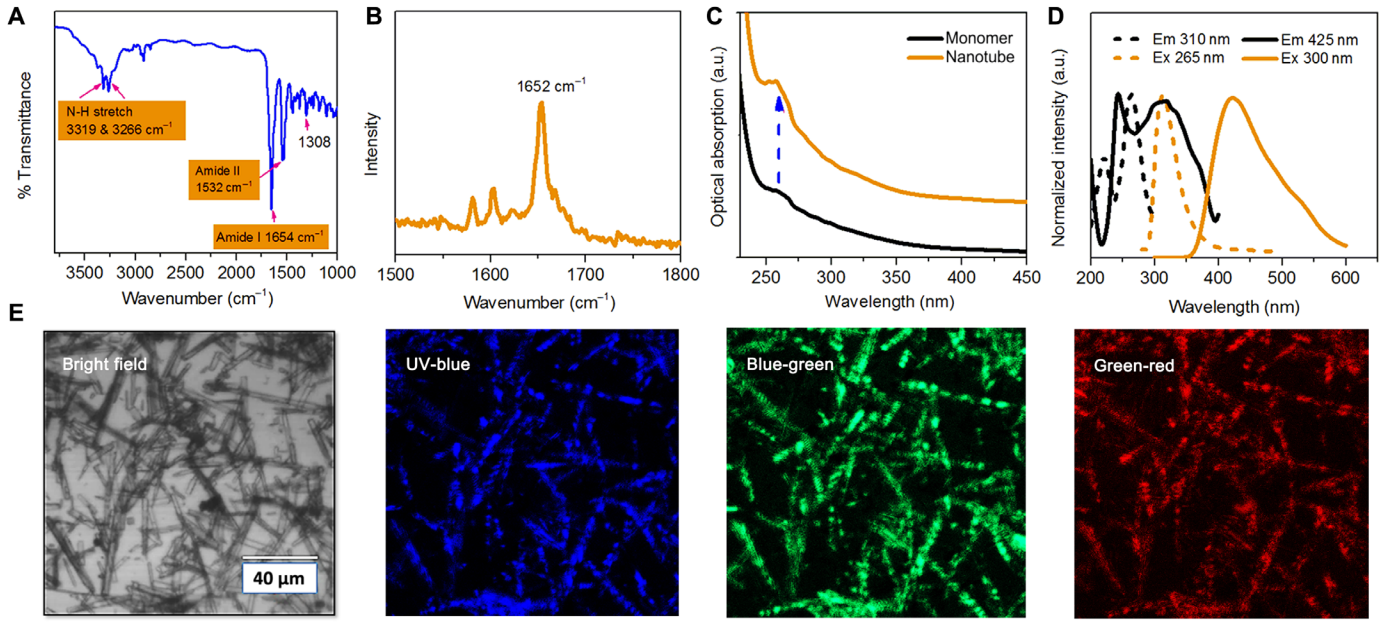

Fig. 3. Characterization of self-assembly behavior in BDCP-1-R nanomaterials. (**A**) FTIR spectrum of the amide bond bands and hydrogen bond region (inset) and (**B**) Raman spectrum of BDCP-1-R peptide nanomaterials. (**C**) UV-vis spectra of BDCP-1-R monomers (black line) and peptide nanomaterials (blue dashed line). a.u., arbitrary units. (**D**) Fluorescence spectra of BDCP-1-R monomers (dashed lines) and peptide nanomaterials (solid lines) dissolved or dispersed in water (1 mg/ml, 20°C). Peptide nanomaterial peaks are broader and red-shifted. (**E**) Optical image of BDCP-1-R peptide nanomaterials and associated fluorescence images with visible luminescence using UV-blue, blue-green, and green-red filters.

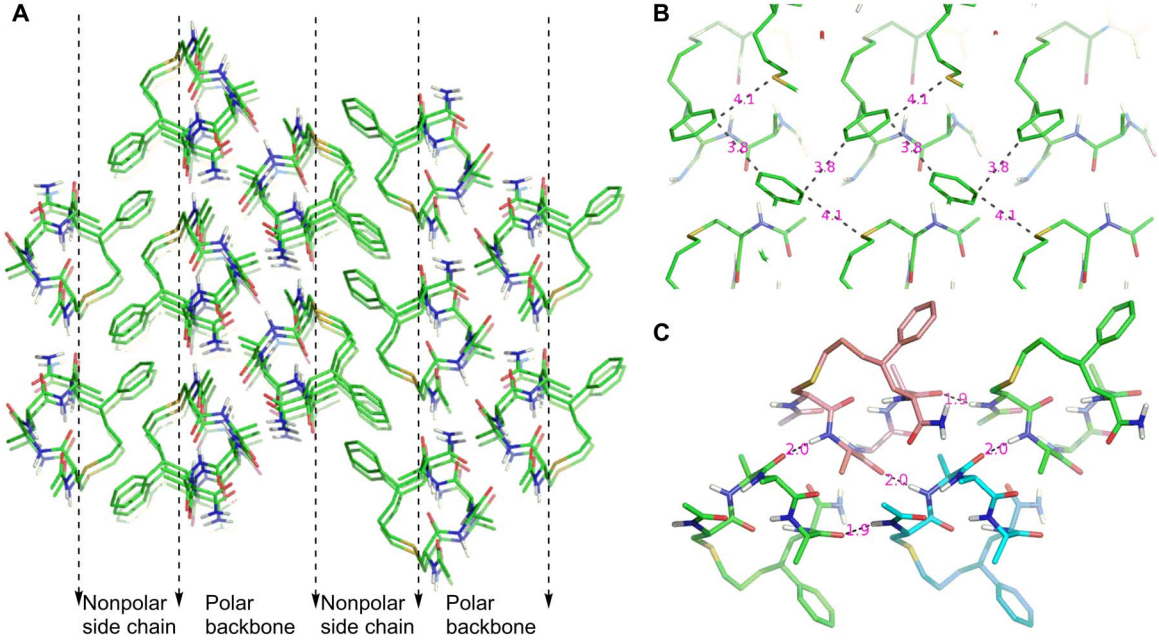

Fig. 4. Elucidation of BDCP-1-R nanostructure packing model. (**A**) Predicted crystallite packing of BDCP-1-R molecules. (**B**) Nonpolar region formed by the aromatic-aromatic and aromatic-sulfur interactions of the side-chain tethers. (**C**) Polar region formed by hydrogen bonding of the α-helical backbones. Carbon atoms in different molecules are shown in different colors. In all the structures, N/O/S atoms are in blue/red/yellow, respectively, and nonpolar hydrogen atoms are omitted for clarity.

interpeptide hydrogen bond networks (Fig. 4C). Unlike previously reported superhelical assemblies with only head-to-tail hydrogen bonding (*19*), the assembly here had zipper-like interlocked patterns with one molecule forming hydrogen bonds simultaneously with four other molecules. In each polar layer, all α-helical peptides were aligned with their macrodipoles in similar directions. Thus, the hydrogen bonds were strengthened by cooperative long-range electrostatics and polarization effects (*36*). In addition, two nearby polar layers (intermitted by one nonpolar layer) have macrodipoles in opposite directions, which eliminate the dipole moment of the whole crystallite.

Extending sequence scope of the self-assembly

To examine the de novo nature of this assembly process, the assembly of other sequences, including Ac-CAGAS$_5$(Ph)-NH$_2$ (BDCP-3-S/R) and Ac-CAVAS$_5$(Ph)-NH$_2$ (BDCP-4-S/R), was examined under the same conditions (Fig. 5A). As expected, both BDCP-3-R and BDCP-4-R assembled whereas their S epimers did not. CD (Fig. 5C) indicated BDCP-3-S and BDCP-4-S were nonhelical, whereas their R isomers adopted helical conformations in solution. The SEM images (Fig. 5B) revealed BDCP-3-R and BDCP-4-R formed flower- or ribbon-shaped structures. The FTIR also confirmed that BDCP-3-R and BDCP-4-R adopted an α helix structure when assembled. Therefore, the above results suggest that our strategy may allow de novo assembly of peptides, where the resulting detailed nanostructures are sequence-dependent. This provides a broad chemical space for developing materials with different nanostructures for different purposes.

Application of CIH peptide nanomaterials in electrochemical supercapacitors

Constraint peptides are known for their superior chemical and thermal stability compared to their linear counterparts (*22*). The nanomaterials assembled from constrained helical peptides are therefore highly promising for use in bionanotechnology applications because their properties could be tuned using sequence variation (*12*). One possible application is in biocompatible supercapacitors (*37*–*41*), where the use of biocompatible active materials could extend their applications to wearable, implantable, and biodegradable devices (*42*). Here, we demonstrated the BDCP nanomaterials were excellent candidate materials for supercapacitors and, therefore, are promising for use in biocompatible energy devices.

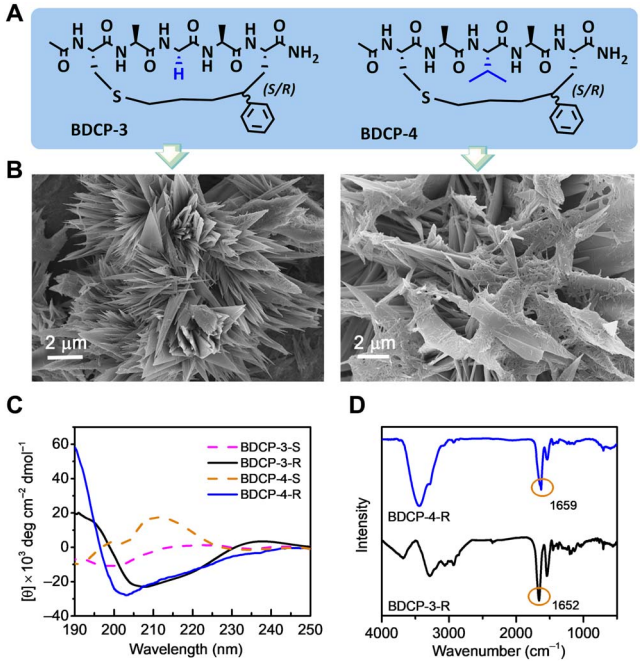

Fig. 5. CIH peptide assembly is tolerant of amino acid mutations. (**A**) Molecular structures of BDCP-3(R/S) and BDCP-4(R/S). Side chains of middle amino acids are labeled in blue. (**B**) SEM images of self-assembled BDCP-3-R and BDCP-4-R. (**C**) CD spectra of BDCP-3/4-R/S in water (pH 7, 20°C, and 100 μM). (**D**) FTIR spectra of BDCP-3-R and BDCP-4-R. Wavenumbers of peaks in pink circles are given.

The supercapacitor behavior of the BDCP-1-R nanomaterials was investigated by loading the assemblies onto a glassy carbon (GC) working electrode (1 mg/cm^2). The peptide nanomaterial morphology on the electrode was characterized using optical microscopy and SEM. The image in fig. S3A is a macroscopic view of the peptide-modified electrode. The images in fig. S3 (B to D) show the microscopic details of the peptide assemblies, where peptide hollow tubes and solid belts were both observed, consistent with the characterized morphology. Cyclic voltammetry (CV) measurements were obtained using a three-electrode cell in 0.05 M KH_2PO_4/0.5 M KCl at room temperature (fig. S4A). Figure 6A presents the CV curves for BDCP-1-R peptide assemblies at different scan rates ranging from 10 to 80 mV/s with a voltage range of 0 to 1 V (versus Hg/HgO). The curves exhibited typical capacitor shapes. A control experiment using a bare GC electrode confirmed that the capacitance could largely be attributed to the peptide nanomaterials. Typical capacitive charge-discharge curves of the peptide-loaded electrode are shown in Fig. 6B, with galvanostatic current densities ranging from 50 to 200 μA/cm^2. The capacitance retention was found to be ~80% after 5000 cycles, as shown in Fig. 6C, demonstrating the excellent electrochemical stability of the peptide nanomaterials.

Because peptide morphology can influence energy storage capacity, we also studied the relationships between peptide sequence, morphology, and energy storage capacity. We performed CV measurements for peptides BDCP-2-R to BDCP-4-R (fig. S4, B to D). These peptides had different areal capacitances that trended 2 > 1 > 3 > 4 (Fig. 6D). The galvanostatic charging/discharging of BDCP-2-R to BDCP-4-R was also performed (data shown in fig. S4, E to G), and the areal capitances were calculated and plotted versus current density in Fig. 6E. In particular, peptide BDCP-2-R had an areal capacitance of 2.35 mF/cm^2 at a current density of 50 μA/cm^2. We also investigated the influence of the electrolyte on capacitance and found the capacitance could be further increased by using 0.1 M H_2SO_4 instead of 0.05 M KH_2PO_4 and 0.5 M KCl (fig. S5A) (*37*). We observed the morphology of peptide assemblies on the electrode after CV measurement. We found that the peptide nanostrucutures revealed little change compared to that before CV measurement (Fig. 5, B to D). These results suggest that the peptide nanomaterials are very stable in different electrolytes. Figure 6H compares the areal capacitance of the reported peptide-based supercapacitors and presents the clear improvement in areal capacitance in this work.

DISCUSSION

In summary, we demonstrated cyclized helical peptides can self-assemble into well-ordered nanostructures. This is a novel self-assembly mode for peptides. The self-assembly was controlled by an in-tether substituent group. Whereas the absolute configuration of the chiral center determined the helicity, the aromaticity of the chiral center was the driving force for self-assembly. As a proof of principle, self-assembled BDCP-1-R peptide nanostructures were carefully characterized to confirm the building blocks of the BDCP-1-R peptides in the nanostructures. Theoretical calculations suggest the existence of interpeptide π-π and π-sulfur interactions and hydrogen bond networks in the BDCP-1-R self-assembly.

The self-assembled peptide nanomaterials also performed excellently as biocompatible active materials in electrochemical supercapacitors, which are promising for use in wearable, implantable, and biodegradable devices. We systematically studied the energy storage capacity of the peptide nanomaterials for use in electrochemical

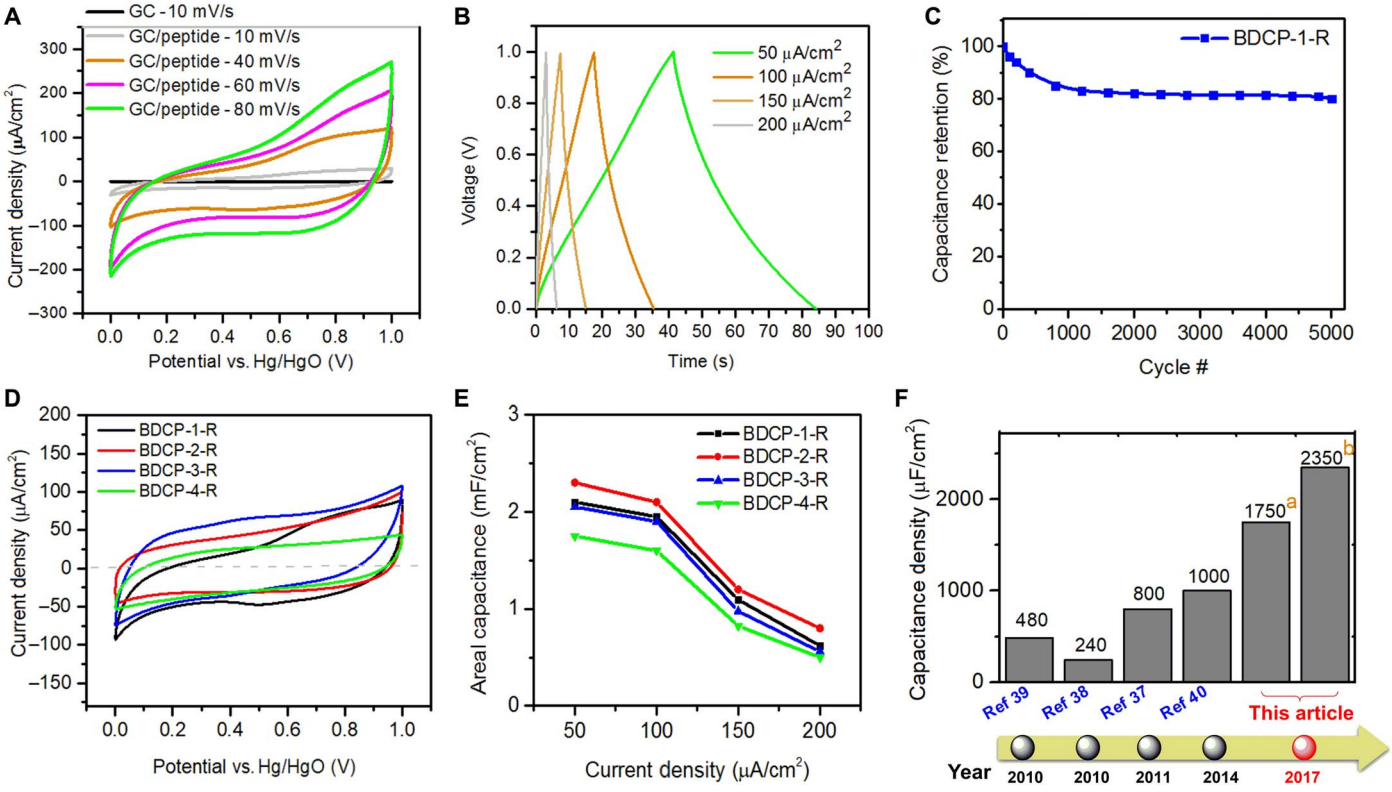

Fig. 6. Characterization of peptide nanostructures as supercapacitors. (**A**) Cyclic voltammograms at different scan rates for BCDP-1-R. (**B**) Galvanostatic charge-discharge curves of BDCP-1-R at different current densities. (**C**) Cycle stability of BDCP-1-R electrode at a scan rate of 0.4 mV/s with 5000 cycles. (**D**) CV curves for peptides BDCP-1-R through BDCP-4-R at a scan rate of 10 mV/s. (**E**) Areal capacitances as functions of current density. (**F**) Comparison of reported peptide-based supercapacitors. a, areal capacitance of BDCP-4-R at 50 μA/cm^2; b, areal capacitance of BDCP-2-**R** at 50 μA/cm^2.

supercapacitors for the first time. Areal capacitance was significantly improved compared to previously published literature.

The concept of de novo self-assembly reported in the present study could be extended to peptide sequences. We therefore envision the novel self-assembly mode of cyclized helical peptides will have broad and important applications in bionanoscience and technology.

MATERIALS AND METHODS

Peptide synthesis and self-assembly

Peptide synthesis was performed manually on Rink amide MBHA resin (loading capacity, 0.54 mmol/g; GL Biochem Co. Ltd) using standard Fmoc-based solid-phase peptide synthesis. Briefly, Rink amide AM resin was preswelled with 1:1 dichloromethane (DCM)/*N*-methyl-2-pyrrolidone (NMP) for 30 min. Fmoc deprotection was performed with 50% morpholine in NMP for 30 min twice. The resin was washed with NMP five times, DCM five times, and then NMP five times. Fmoc-protected amino acids (6.0 equiv. according to initial loading of the resin) and 2-(6-chloro-1*H*-benzotriazole-1-yl)-1,1,3,3-tetramethylaminium hexafluorophosphate (5.9 equiv.) were dissolved in NMP and then in *N*,*N*-diisopropylethylamine (12.0 equiv.). The mixture was preactivated for 1 min and added to the resin for 1 to 2 hours, and then the resin was washed with NMP (five times), DCM (five times), and NMP (five times). Upon completion of peptide synthesis, peptides were N-terminally acetylated by incubating in a 1:1:8 by volume solution of acetic anhydride, *N*,*N*-diisopropylethylamine, and NMP for 1 hour. Peptides were cleaved from the resin with a mixture of trifluoroacetic acid/H_2O/EDT/TIS (94:2.5:2.5:1) for 2 hours and concentrated under a stream of nitrogen. The crude peptides were then precipitated with 1:1 by volume hexane/Et_2O at −20°C, isolated by centrifugation, dissolved in water/acetonitrile, purified by semipreparative high-performance liquid chromatography, and analyzed by liquid chromatography–mass spectrometry (LC-MS). Lyophilized pentapeptide powder was dissolved in deionized (DI) water (2 mg/ml). The concentrated peptide solutions were then sonicated for 10 min, and the pentapeptides were assembled into nanostructures.

CD spectroscopy

CD spectra were recorded using a Chirascan Plus Circular Dichroism Spectrometer (Applied Photophysics) at 20°C. Peptides were dissolved in 300 μl of ddH_2O at a final concentration of 0.10 mM. The parameters used in this experiment were wavelengths from 250 to 190 nm measured at a resolution of 0.5 nm and a scan speed of 0.5 nm/s. Each sample was scanned twice, and the averaged spectrum was smoothed using the Pro-Data Viewer by Applied Photophysics with a smooth window of 10. CD data were presented as mean residual ellipticity [θ] in deg cm^2 dmol^{-1}. The concentration of each sample was calculated as absorption (optical density) at 280 nm × dilution factor ÷ 1 (cm) ÷ 1490 (1 cm^{-1} M^{-1}) × 1000 (mM^{-1}) = concentration (mM).

X-ray diffraction

BDCP-1 was mounted vertically onto the goniometer of an Oxford Instruments Gemini X-ray diffractometer equipped with a Sapphire 3 charge-coupled device (CCD) detector. The sample-to-detector distance

was 45 mm. CLEARER software was used to reduce the two-dimensional data to a one-dimensional intensity profile. The peptide structures of the samples were studied using a PAN analytical X'Pert X-ray diffractometer with Cu Kα radiation. The sample powders were scanned in the range of 2θ = 2° to 60° with a step size of 0.02°.

FTIR spectroscopy

To characterize interactions within the samples, qualitative analysis was performed by analyzing the infrared absorption spectrum of each sample. KBr pellets were prepared before measurement. A Bruker Vertex 70 FTIR spectrometer was used for FTIR analysis with a wavenumber ranging from 4000 to 400 cm^{-1}.

High-resolution TEM

Samples (10 μl) of peptide assemblies were sonicated in a bath sonicator for 5 s. The samples were placed on Formvar/carbon mesh 400 copper grids (Electron Microscopy Sciences) for 20 s and then removed using nitrocellulose paper. The Cu grids were left to dry at room temperature. TEM images were recorded using a high-resolution transmission electron microscope (JEM-100F; 200 kV).

Scanning electron microscopy

Pentapeptide samples were placed on silicon slides and left to dry at room temperature. Samples were then viewed using a scanning electron microscope (ZEISS Supra 55, Oxford X-Max 20; 20 kV).

Atomic force microscopy

Pentapeptide solutions were prepared at a concentration of 5 mg/ml. A droplet of solution was placed on a siliconized glass for more than 30 min to allow volatilization of the solvent. Large areas were imaged at different magnifications using an optical microscope (Axio Imager, Carl Zeiss). AFM analysis was carried out using a Bruker AFM multimode (MultiMode 8, Bruker). The probes used for AFM were antimony-doped (n) silicon cantilevers with a spring constant of 40 N/m (Bruker) and resonance frequency of 300 kHz. Observation was performed using tapping mode with a scan rate of 0.9 Hz. After acquiring the AFM images, pentapeptide data were analyzed using the NanoScope Analysis program.

Characterization of PL

Measurements of PL and PLE were performed using a Horiba Jobin Yvon FL3-11 spectrofluorometer. PL/PLE measurements were taken of peptide nanofibers and monomers on a standard cuvette. Fluorescence measurements of peptide nanofiber film were acquired on a glass coverslip.

Raman spectroscopy

Raman data were acquired using a Horiba Jobin-Yvon LabRam Aramis Raman spectrometer. A 532-nm Ar-ion laser was used as the excitation source, and the substrate plate was stainless steel with no Raman signal, guaranteeing a fluorescence-free background. Wavenumbers ranging from 200 to 3000 cm^{-1} were scanned, and each spectrum was acquired for 60 s. The analysis was executed for more than three points for each sample for reproducibility and reliability.

UV-vis spectroscopic analysis

UV-vis spectra were obtained using an Otsuka Electronics MCPD 7000 UV-visible spectrophotometer with fiber optics and an ultra-high sensitive CCD array cooled by a Peltier device. The sample room was a custom-made dark box in which versatile measurements, including transmission measurements of LB films, could be performed. Transmitted light was collected through an integral sphere. For visible spectrometric measurements, a quartz plate was used, which was purchased from the same provider as the germanium substrate.

Computational modeling of peptide crystal structure

Crystal structure prediction was performed in the cloud platform of XtalPi Inc., which integrates conformation analysis, force-field parameterization, crystal structure searching, clustering, and ranking. The crystal packings were sampled in the five most frequent space groups ($P2_1$, $P2_12_12_1$, P1, C2, and $P2_12_12$) according to the Cambridge structural database statistics for all chiral entries. The searching space included lattice parameters, molecular positions and orientations, and rotations along some single bonds. Initially, the lattice energies were evaluated using a system-specific force field. Finally, the geometries and energies were reoptimized using the Perdew-Burke-Ernzerhof functional with dispersion correction using VASP software.

Preparation of GC/peptide electrode and electrochemical measurements

A GC electrode (3 mm in diameter) was polished to be mirror-like using 0.05 μm of alumina medium and then coated with a layer of active materials to serve as a working electrode. The active material ink was prepared as follows: 2 mg of peptide was dispersed in 1 ml of DI water. Nafion [80 μl, obtained as a 5 wt % (weight %) solution; Electrochem Inc.] was added, and the mixture was sonicated for 30 min to form a homogeneous ink. The resulting ink (5 μl) was drop-cast onto the GC electrode and subsequently air-dried to obtain a mass loading of 1 mg/cm^2. The electrode was tested on a CHI 660e electrochemical workstation (Chenhua) in three-electrode electrochemical cells using 0.05 M KH_2PO_4/0.5 M KCl or 0.1 M H_2SO_4. Pt wire and Hg/HgO were used as the counter and reference electrodes, respectively. For the GC/peptide electrode, the areal capacitance (F/cm^2) was calculated from the charging/discharging curves using the equation $Cv = I\Delta t/S\Delta V$, where I refers to the discharging current (A), S is the geometrical area of the glass carbon (cm^2), Δt is the discharging time (s), and ΔV is the potential window (V).

SUPPLEMENTARY MATERIALS

Supplementary material for this article is available at http://advances.sciencemag.org/cgi/content/full/4/5/eaar5907/DC1

Synthesis of BDCP peptides

LC-MS, mass, and ^1H and ^{13}C spectra for nonnatural amino acids or peptides

BDCP-2-S/R

BDCP-3-S/R

BDCP-4-S/R

Nuclear magnetic resonance data of unnatural amino acids

^1H of Fmoc-S_5(2-Me)-OH

^{13}C of Fmoc-S_5(2-Me)-OH

High-resolution mass spectrum

^1H of Fmoc-S_5(2-Ph)-OH

^{13}C of Fmoc-S_5(2-Ph)-OH

High-resolution mass spectrum

^1H of Fmoc-S_5(2-naphnal)-OH

fig. S1. CD spectra of BDCP-0/1/2/-R or S in water, respectively.

fig. S2. Simulated powder XRD pattern from the predicted crystal structure of BDCP-1-R.

fig. S3. Morphology of the BDCP-1-R nanostructure on GC electrode.

fig. S4. Electrochemical performance of the BDCP-2/3/4-R peptide assemblies.

fig. S5. Electrochemical performance of BDCP-1-R nanostructures in different electrolytes.

table S1. Relationship between peptide structures and self-assemblies.

cif file

REFERENCES AND NOTES

1. T. G. Barclay, K. Constantopoulos, J. Matisons, Nanotubes self-assembled from amphiphilic molecules via helical intermediates. *Chem. Rev.* **114**, 10217–10291 (2014).
2. Z. Luo, S. Zhang, Designer nanomaterials using chiral self-assembling peptide systems and their emerging benefit for society. *Chem. Soc. Rev.* **41**, 4736–4754 (2012).
3. J. Wang, K. Liu, R. Xing, X. Yan, Peptide self-assembly: Thermodynamics and kinetics. *Chem. Rev.* **45**, 5589–5604 (2016).
4. R. G. Ellis-Behnke, Y.-X. Liang, S.-W. You, D. K. C. Tay, S. Zhang, K.-F. So, G. E. Schneider, Nano neuro knitting: Peptide nanofiber scaffold for brain repair and axon regeneration with functional return of vision. *Proc. Natl. Acad. Sci. U.S.A.* **103**, 5054–5059 (2006).
5. A. L. Boyle, D. N. Woolfson, De novo designed peptides for biological applications. *Chem. Soc. Rev.* **40**, 4295–4306 (2011).
6. J. H. Kim, M. Lee, J. S. Lee, C. B. Park, Self-assembled light-harvesting peptide nanotubes for mimicking natural photosynthesis. *Angew. Chem. Int. Ed. Engl.* **51**, 517–520 (2012).
7. K. Tao, P. Makam, R. Aizen, E. Gazit, Self-assembling peptide semiconductors. *Science* **358**, eaam9756 (2017).
8. I. W. Hamley, Peptide nanotubes. *Angew. Chem. Int. Ed. Engl.* **53**, 6866–6881 (2014).
9. S. E. Paramonov, H.-W. Jun, J. D. Hartgerink, Self-assembly of peptide–amphiphile nanofibers: The roles of hydrogen bonding and amphiphilic packing. *J. Am. Chem. Soc.* **128**, 7291–7298 (2006).
10. A. Aggeli, M. Bell, N. Boden, J. N. Keen, P. F. Knowles, T. C. B. McLeish, M. Pitkeathly, S. E. Radford, Responsive gels formed by the spontaneous self-assembly of peptides into polymeric β-sheet tapes. *Nature* **386**, 259–262 (1997).
11. I. C. Tanrikulu, A. Forticaux, S. Jin, R. T. Raines, Peptide tessellation yields micrometre-scale collagen triple helices. *Nat. Chem.* **8**, 1008–1014 (2016).
12. L. Adler-Abramovich, E. Gazit, The physical properties of supramolecular peptide assemblies: From building block association to technological applications. *Chem. Soc. Rev.* **43**, 6881–6893 (2014).
13. B. Sun, Q. Li, H. Riegler, S. Eickelmann, L. Dai, Y. Yang, R. Perez-Garcia, Y. Jia, G. Chen, J. Fei, K. Holmberg, J. Li, Self-assembly of ultralong aligned dipeptide single crystals. *ACS Nano* **11**, 10489–10494 (2017).
14. R. Chapman, M. Danial, M. L. Koh, K. A. Jolliffe, S. Perrier, Design and properties of functional nanotubes from the self-assembly of cyclic peptide templates. *Chem. Soc. Rev.* **41**, 6023–6041 (2012).
15. J. Kim, S. Kwon, S. H. Kim, C.-K. Lee, J.-H. Lee, S. J. Cho, H.-S. Lee, H. Ihee, Microtubes with rectangular cross-section by self-assembly of a short β-peptide foldamer. *J. Am. Chem. Soc.* **134**, 20573–20576 (2012).
16. V. Azzarito, K. Long, N. S. Murphy, A. J. Wilson, Inhibition of α-helix-mediated protein–protein interactions using designed molecules. *Nat. Chem.* **5**, 161–173 (2013).
17. X. Chen, Y. He, Y. Kim, M. Lee, Reversible, short α-peptide assembly for controlled capture and selective release of enantiomers. *J. Am. Chem. Soc.* **138**, 5773–5776 (2016).
18. J. Lee, I. R. Choe, N.-K. Kim, W.-J. Kim, H.-S. Jang, Y.-S. Lee, K. T. Nam, Water-floating giant nanosheets from helical peptide pentamers. *ACS Nano* **10**, 8263–8270 (2016).
19. S. Mondal, L. Adler-Abramovich, A. Lampel, Y. Bram, S. Lipstman, E. Gazit, Formation of functional super-helical assemblies by constrained single heptad repeat. *Nat. Commun.* **6**, 8615 (2015).
20. H. J. Dyson, P. E. Wright, Defining solution conformations of small linear peptides. *Annu. Rev. Biophys. Biophys. Chem.* **20**, 519–538 (1991).
21. S. Sim, Y. Kim, T. Kim, S. Lim, M. Lee, Directional assembly of α-helical peptides induced by cyclization. *J. Am. Chem. Soc.* **134**, 20270–20272 (2012).
22. Y. H. Lau, P. de Andrade, Y. Wu, D. R. Spring, Peptide stapling techniques based on different macrocyclisation chemistries. *Chem. Soc. Rev.* **44**, 91–102 (2015).
23. J. C. Phelan, N. J. Skelton, A. C. Braisted, R. S. McDowell, A general method for constraining short peptides to an α-helical conformation. *J. Am. Chem. Soc.* **119**, 455–460 (1997).
24. K. Hu, H. Geng, Q. Zhang, Q. Liu, M. Xie, C. Sun, W. Li, H. Lin, F. Jiang, T. Wang, Y.-D. Wu, Z. Li, An in-tether chiral center modulates the helicity, cell permeability, and target binding affinity of a peptide. *Angew. Chem. Int. Ed. Engl.* **55**, 8013–8017 (2016).
25. Y. Jiang, K. Hu, X. Shi, Q. Tang, Z. Wang, X. Ye, Z. Li, Switching substitution groups on the in-tether chiral centre influences backbone peptides' permeability and target binding affinity. *Org. Biomol. Chem.* **15**, 541–544 (2017).
26. K. Hu, C. Sun, D. Yang, Y. Wu, C. Shi, L. Chen, T. Liao, J. Guo, Y. Liu, Z. Li, A precisely positioned chiral center in an *i*, *i* + 7 tether modulates the helicity of the backbone peptide. *Chem. Commun.* **53**, 6728–6731 (2017).
27. A. C. Santos, P. Pattekari, S. Jesus, F. Veiga, Y. Lvov, A. J. Ribeiro, Sonication-assisted layer-by-layer assembly for low solubility drug nanoformulation. *ACS Appl. Mater. Interfaces* **7**, 11972–11983 (2015).
28. N. Amdursky, M. Molotskii, E. Gazit, G. Rosenman, Elementary building blocks of self-assembled peptide nanotubes. *J. Am. Chem. Soc.* **132**, 15632–15636 (2010).
29. D. A. Middleton, J. Madine, V. Castelletto, I. W. Hamley, Insights into the molecular architecture of a peptide nanotube using FTIR and solid-state NMR spectroscopic measurements on an aligned sample. *Angew. Chem. Int. Ed. Engl.* **52**, 10537–10540 (2013).
30. J. D. Hartgerink, J. R. Granja, R. A. Milligan, M. R. Ghadiri, Self-assembling peptide nanotubes. *J. Am. Chem. Soc.* **118**, 43–50 (1996).
31. M. Pellach, S. Mondal, L. J. W. Shimon, L. Adler-Abramovich, L. Buzhansky, E. Gazit, Molecular engineering of self-assembling diphenylalanine analogues results in the formation of distinctive microstructures. *Chem. Mater.* **28**, 4341–4348 (2016).
32. H. Xu, A. K. Das, M. Horie, M. S. Shaik, A. M. Smith, Y. Luo, X. Lu, R. Collins, S. Y. Liem, A. Song, P. L. A. Popelier, M. L. Turner, P. Xiao, I. A. Kinloch, R. V. Ulijn, An investigation of the conductivity of peptide nanotube networks prepared by enzyme-triggered self-assembly. *Nanoscale* **2**, 960–966 (2010).
33. N. C. Burgess, T. H. Sharp, F. Thomas, C. W. Wood, A. R. Thomson, N. R. Zaccai, R. L. Brady, L. C. Serpell, D. N. Woolfson, Modular design of self-assembling peptide-based nanotubes. *J. Am. Chem. Soc.* **137**, 10554–10562 (2015).
34. S. K. Burley, G. A. Petsko, Aromatic-aromatic interaction: A mechanism of protein structure stabilization. *Science* **229**, 23–28 (1985).
35. R. J. Zauhar, C. L. Colbert, R. S. Morgan, W. J. Welsh, Evidence for a strong sulfur–aromatic interaction derived from crystallographic data. *Biopolymers* **53**, 233–248 (2000).
36. Y.-D. Wu, Y.-L. Zhao, A theoretical study on the origin of cooperativity in the formation of 3_{10}- and α-helices. *J. Am. Chem. Soc.* **123**, 5313–5319 (2001).
37. P. Beker, G. Rosenman, Bioinspired nanostructural peptide materials for supercapacitor electrodes. *J. Mater. Res.* **25**, 1661–1666 (2010).
38. P. Beker, I. Koren, N. Amdursky, E. Gazit, G. Rosenman, Bioinspired peptide nanotubes as supercapacitor electrodes. *J. Mater. Sci.* **45**, 6374–6378 (2010).
39. L. Adler-Abramovich, D. Aronov, P. Beker, M. Yevnin, S. Stempler, L. Buzhansky, G. Rosenman, E. Gazit, Self-assembled arrays of peptide nanotubes by vapour deposition. *Nat. Nanotechnol.* **4**, 849–854 (2009).
40. J. Zhang, X. Wu, Z. Gan, X. Zhu, Y. Jin, Unidirectionally aligned diphenylalanine nanotube/microtube arrays with excellent supercapacitive performance. *Nano Res.* **7**, 929–937 (2014).
41. A. Lampel, S. A. McPhee, H.-A. Park, G. G. Scott, S. Humagain, D. R. Hekstra, B. Yoo, P. W. J. M. Frederix, T.-D. Li, R. R. Abzalimov, S. G. Greenbaum, T. Tuttle, C. Hu, C. J. Bettinger, R. V. Ulijn, Polymeric peptide pigments with sequence-encoded properties. *Science* **356**, 1064–1068 (2017).
42. V. Nguyen, R. Zhu, K. Jenkins, R. Yang, Self-assembly of diphenylalanine peptide with controlled polarization for power generation. *Nat. Commun.* **7**, 13566 (2016).

Acknowledgments

Funding: We acknowledge financial support from the Natural Science Foundation of China (grants 21778009, 81701818, and 51673029), Ministry of Science and Technology of China (2015DFA31590), and the Shenzhen Science and Technology Innovation Committee (JCYJ20170412150719814 and GJHS20170310093122365). **Author contributions:** K.H. and Z.G.L. conceived and designed the experiments. K.H., Y.J., and F.Y. synthesized and characterized the peptide nanomaterial. P.-Y.Z., H.G., and F.J. performed the computational modeling. K.H., Y.J., W.X., and H.L. performed the electrochemical experiments. K.H., Y.J., W.X., F.J., X.W., Q.L.Z., Z.G.L., and Z.L. wrote the manuscript. All authors participated in discussions on the data and critiques of the manuscript. **Competing interests:** The authors declare that they have no competing interests. **Data and materials availability:** All data needed to evaluate the conclusions in the paper are present in the paper and/or the Supplementary Materials. Additional data related to this paper may be requested from the authors.

Submitted 27 November 2017
Accepted 28 March 2018
Published 11 May 2018
10.1126/sciadv.aar5907

Citation: K. Hu, Y. Jiang, W. Xiong, H. Li, P.-Y. Zhang, F. Yin, Q. Zhang, H. Geng, F. Jiang, Z. Li, X. Wang, Z. Li, Tuning peptide self-assembly by an in-tether chiral center. *Sci. Adv.* **4**, eaar5907 (2018).

Tuning peptide self-assembly by an in-tether chiral center

Kuan Hu, Yixiang Jiang, Wei Xiong, Hu Li, Pei-Yu Zhang, Feng Yin, Qianling Zhang, Hao Geng, Fan Jiang, Zhou Li, Xinwei Wang and Zigang Li

Sci Adv **4** (5), eaar5907.
DOI: 10.1126/sciadv.aar5907